



PERGAMON

Available online at www.sciencedirect.com

SCIENCE @ DIRECT®

Scripta Materialia 48 (2003) 881–887



www.actamat-journals.com

The kinetics of nanocrystallization and microstructural observations in FINEMET, NANOPERM and HITPERM nanocomposite magnetic materials

M.E. McHenry^{a,*}, F. Johnson^a, H. Okumura^a, T. Ohkubo^a,
V.R.V. Ramanan^b, D.E. Laughlin^a

^a Department of Materials Science and Engineering, Carnegie Mellon University, 243 Roberts Eng. Hall—5000, Forb., Pittsburgh, PA 15213, USA

^b ABB Inc., Raleigh, NC 27606, USA

Received 31 July 2002; received in revised form 1 November 2002; accepted 1 November 2002

Abstract

This paper presents experimental observations of the nanocrystallization process in materials having Fe–Si (FINEMET), α -Fe (NANOPERM), and α' -FeCo (HITPERM) nanocrystals coupled through an amorphous phase. Crystallization kinetics and chemical partitioning during crystallization are described. Isothermal nanocrystallization is discussed in the framework of the Johnson–Mehl–Avrami–Kolmogorov model and constant heating rate experiments analyzed in the context of the Kissinger model.

© 2003 Acta Materialia Inc. Published by Elsevier Science Ltd. All rights reserved.

Keywords: Nanocomposites; Soft magnets; HITPERM; NANOPERM; FINEMET

1. Introduction

Nanocrystalline magnets are being investigated for transformers, inductors, and high moment underlayers for perpendicular recording media, etc., where low coercivities, H_c , large saturation inductions, B_s , large resistivities and good thermal stability are needed. Superior soft magnetic properties stem from chemical and structural variations on a nanoscale. Important magnets are derived by

crystallizing amorphous precursors resulting in nanocrystalline grains of a (BCC, DO₃ or CsCl) (Fe(Co), X) phase consuming 20–90% of the total volume, homogeneously dispersed in an amorphous matrix. These two-phase materials are designated *metallamorphous nanocomposites*. Applications have been identified utilizing the patented Fe–Si–B–Nb–Cu alloys (tradename FINEMET@TM [1]) and FeMBCu, alloys (tradename NANOPERM@TM [2]). CMU efforts under AFOSR(ONR) MURI funding, resulted a new nanocrystalline (Fe_{1-x}Co_x)₈₈M₇B₄Cu (M = Nb, Zr, Hf) soft magnetic material called HITPERM [3]. HITPERM has high frequency response and high temperature induction. Magnetic metal/amorphous

* Corresponding author. Tel.: +1-412-268-2703; fax: +1-412-268-3113.

E-mail address: mm7g@andrew.cmu.edu (M.E. McHenry).

nanocomposites [4] have excellent soft magnetic properties as measured by the figures of merit of combined induction and magnetic permeability. Other figures of merit include high frequency magnetic response and retention of magnetic softness at elevated temperatures. Frequency response is ultimately limited by Snoek's law and uniaxial anisotropy must be developed in a controlled manner to attain the high frequency limit. High temperature operation is advantageous either to allow integration with other high temperature electronic components or to allow greater efficiency in going to higher frequency.

Averaging magnetocrystalline anisotropy over grains coupled within an *exchange length* is the root of magnetic softness in these materials [5,6]. In HITPERM nanocomposites [4] nanocrystalline α and α' (B2)-FeCo are formed with improved high temperature magnetic properties. Here we the following fundamental issues: (1) models of the kinetics of nanocrystallization; (2) observations of the role of chemical partitioning occurring during crystallization in determining the temperature dependence of the intergranular coupling of the nanocrystals. HITPERM has been developed for applications with high permeability requirements and with needs for large inductions at high temperatures.

2. Crystallization and nanocrystallization kinetics

Crystallization is a solid state phase transformation often controlled by nucleation and growth kinetics. The progress of an isothermal phase transformation is represented by plotting the volume fraction (i.e. of the primary crystallites) transformed, $X(t, T)$, as a function of temperature, T , and time, t , in a *TTT curve*. The reaction kinetic arguments necessary to derive a TTT curve are based on Johnson–Mehl [7]–Avrami [8]–Kolmogorov [9] (Johnson–Mehl–Avrami–Kolmogorov (JMAK) kinetics). The JMAK model for isothermal (primary) crystallization kinetics considers modifications to simple first-order reaction rate kinetics, where the rate of transformation depends linearly on the volume fraction of parent

phase remaining, $(1 - X(t))$, with a rate constant k which is thermally activated:

$$k = k_0 \exp\left(\frac{-Q^*}{k_B T}\right) \quad (1)$$

and Q^* is the activation energy barrier to crystallization. Modifications within JMAK consider (1) the dimensionality of the growing particle; (2) the time dependence of the nucleation rate, (3) whether growth is linear or parabolic and (4) the eventual impingement of growing particles at long times. The JMAK equation, for $X(t)$, is written in the general form:

$$X = 1 - \exp(- (k(t - t_i))^n) \quad (2)$$

where t_i is an incubation time, the exponent n is observed to vary between 1 and 4 and is used to corroborate a nucleation and growth mechanism and dimensionality. From determination of $X(t)$ at various temperatures $k(T)$ can be determined and Q_{JMA}^* inferred from the Arrhenius Eq. (1). Kissinger plots [10] are also often used to determine activation energies for crystallization, Q_K^* .

The JMAK model gives a representation with predictive capability of the nanocrystallization kinetics for NANOPERM alloys as originally discussed by Suzuki et al. [11]. It should be noted that the assumptions of the JMAK model do not completely represent the micromechanisms for nanocrystallization [12]. In particular, the slowing down of the rate of transformation at longer times in JMAK is attributed to growth from *phantom nuclei* in the already transformed volume and extended volume to account for the eventual impingement of the growing nanocrystals. It is now clear that the slowing down of the nanocrystallization rate is due to the redistribution of early transition metal (and metalloid) species to the intergranular amorphous phase where it plays the role of a diffusion barrier to further growth of the nanocrystalline phase. Future kinetic models need to be re-examined in light of early transition metal redistribution and so-called *soft impingement*. The decreasing rate of transformation at long times is attributed to impingement of diffusion fields (i.e. early transition metals) surrounding growing nanoparticles rather than the particles themselves.

Microscopic mechanisms for primary nanocrystallization are at the heart of microstructural control for optimizing magnetic properties in metal/amorphous nanocomposites. In general, alloys are chosen to be of hypoeutectic compositions (to maximize the amount of the high moment transition metal). Primary crystallization gives rise to a two-phase microstructure consisting of the magnetic nanocrystals and an intergranular amorphous phase enriched in early transition metal and metalloids species. A mechanistic model for nucleation and growth has been established in most detail for FINEMET alloys [13,14].

3. Crystallization observations in Fe-based metallic glasses

Typical Metglas alloys are hypoeutectic (Fe-rich), so as to have large inductions, and observed to crystallize in a two-step process involving primary crystallization of α -Fe. The primary crystallization reaction; $\text{Am} \rightarrow \text{Am}' + \alpha\text{-Fe}$; is followed by secondary crystallization of a metalloid enriched amorphous phase; Am' [15]. Luborsky and Lieberman [16] studied crystallization kinetics of $\text{Fe}_x\text{B}_{1-x}$ alloys using differential scanning calorimetry (DSC). Activation energies of ~ 2.5 eV were determined for $x = 72\text{--}82$ independent of x , for $x = 82\text{--}88$ Q_K^* was observed to decrease with x . This indicates the importance of near eutectic compositions for amorphous phase stability. Raman and Fish [17] observed that replacement of B by Si increases activation energy barriers in Metglas alloys, with JMAK morphology indices n ranging from 2.5 to 3.5 consistent with a 3-D nucleation and growth mechanism. Donald and Davies [18] studied the primary crystallization temperature, T_{x1} , as a function of transition metal substitution, X , in $\text{M}_{78-x}\text{X}_x\text{Si}_{10}\text{B}_{12}$. They explained variations in T_{x1} , in the framework of Hume-Rothery rules correlating T_{x1} with the ordering of the cohesive energies of the pure species, X , and atomic size. Two important observations pertinent to the discussion below are: (1) Cu additions which promote nucleation of the primary nanocrystals by clustering resulted in significant reductions in T_{x1} , with additions as small as 0.5–1.0 at.%; (2) Early

transition metals, TE (e.g. Zr, Hf, Mo), additions impede growth (increasing activation energies for diffusion) and result in the largest primary crystallization temperatures.

4. Nanocrystallization of FINEMET alloys

$\text{Fe}_{73.5}\text{Si}_{13.5}\text{B}_9\text{Nb}_3\text{Cu}_1$ alloy compositions have been studied extensively for over a decade. Atom probe analysis and high resolution TEM showed [14] that after short annealing (10 min at 550 °C) Cu clusters in nanometer scale regions. In the optimally heat treated material these Cu rich clusters have increased in size to about 5 nm. Nanocrystals with bcc structure were reported to nucleate around these clusters due to the composition fluctuation. Another model proposed that the Cu clusters catalyze the nucleation of the DO_3 phase (instead of BCC) through providing a low energy interface for heterogeneous nucleation [13]. Nb, which refines the microstructure, is proposed to stabilize the amorphous state slowing the growth of the Fe–Si DO_3 crystallites and to promote Cu clustering by altering the solubility of Cu [13]. The kinetics of Cu clustering and crystallization in FINEMET grades with higher Fe content have also recently been studied [19].

Here we report on FINEMET ribbons with a composition of $\text{Fe}_{73.5}\text{Si}_{16.1}\text{B}_{6.4}\text{Nb}_{2.9}\text{Cu}_{1.1}$ (at.%), which have 2.6 at.% higher Si content (replacing B) than in the original FINEMET composition. Fig. 1, shows the existence of the DO_3 structure as evident from X-ray diffractometry. Data taken with a slow step scan (inset) exhibits superlattice

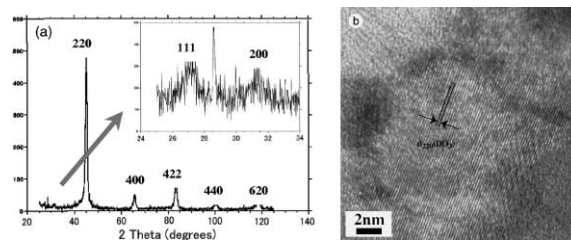


Fig. 1. (a) XRD evidence of DO_3 nanocrystals in annealed $\text{Fe}_{73.5}\text{Si}_{16.1}\text{B}_{6.4}\text{Nb}_{2.9}\text{Cu}_{1.1}$. (b) HREM BF image of one of an ~ 15 nm particle showing lattice fringes of (220) DO_3 planes.

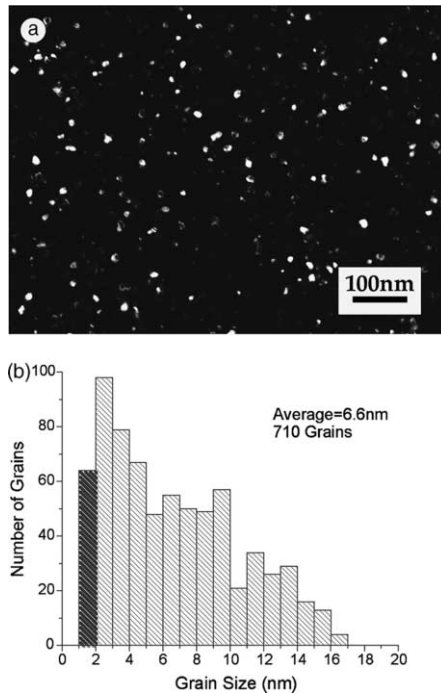


Fig. 2. (a) DF image in sample of Fig. 1 and (b) size distribution of 710 grains.

reflections from (1 1 1) and (2 0 0) planes of the Fe–Si DO_3 structure on the annealed (550 °C for 90 min) ribbons. This confirms the existence of the DO_3 phase although the solid solution of BCC Fe phase with Si may still coexist (the major Bragg peaks exactly coincide with each other). HREM has revealed large quantities of amorphous matrix surrounding ferromagnetic nanocrystals different in composition due to chemical partitioning during nanocrystallization. A HREM image of one of the largest particles (the diameter of ~ 15 nm) with the lattice fringe of (2 2 0) DO_3 planes is shown in Fig. 1(b). The d -value of 0.200–0.201 nm is consistent with X-ray results. The same (1 1 1) and (2 0 0) plane superlattice reflections were observed in selected area electron diffraction pattern of the sample. Nano-probe energy dispersive spectroscopy (EDS) analyses indicate that Cu clusters are often enveloped in nanocrystals consistent with the model of Ayers et al. [13].

TEM bright field (BF) images exhibit a uniform distribution of grains, and an average nanocrystal

grain size of ~ 7 nm as determined from the dark field (DF) image (Fig. 2(a)). The size distribution of 710 grains is shown in Fig. 2(b). The grain morphology appears less spheroidal and less uniform with higher Fe content. For amorphous ribbons slowly heated to 625 °C (just below T_{x2}), a homogeneous 10–25 nm distribution of DO_3 grains is obtained. The composition of the DO_3 phase estimated from its Curie temperature suggests that it regains the original Fe/Si ratio in the amorphous ribbon. From the estimated volume fraction and the magnetization, the intrinsic Fe moment in the DO_3 phase was calculated (considering the moment reduction due to Si neighbors), and shown to be consistent with the data of [20]. The microstructure is dramatically changed when the sample is further heated to 825 °C ($>T_{x2}$).

5. Nanocrystallization of NANOPERM alloys

Vibrating sample magnetometry (VSM), synchrotron X-ray diffractometry (XRD), and DSC have been used to observe crystallization kinetics and results reviewed by Hsiao, et al. [21]. The volume fraction of nanocrystals transformed in the crystallization process was inferred magnetically, thermally and structurally. Constant heating rate, 3-D synchrotron diffraction (Kramer et al. [22], similar studies were performed by Koster, et al. [23] on FINEMET) of the crystallization of NANOPERM ribbon showed the amorphous to nanocrystalline transformation, primary and secondary crystallization phases, and coarsening phenomena. Features included: (1) the appearance of Fe(1 1 0) and Fe(2 0 0) peaks as the primary crystallization of α -Fe occurs at $T_{x1} \sim 510$ °C, (2) T_{x2} occurs at ~ 710 °C with the crystallization of Fe_2Zr and $\text{Fe}_{23}\text{Zr}_6$, (3) the narrowing of the of Fe(1 1 0) and Fe(2 0 0) peaks due to coarsening that occurs after secondary crystallization. Both X-ray and TEM have been used to identify the primary and secondary crystallization reactions, respectively, to be: $\text{Am} \rightarrow \text{Am}' + \alpha\text{-Fe}$; $\text{Am}' \rightarrow \text{Fe}_{23}\text{Zr}_6 + \text{Fe}_2\text{Zr}$. Isothermal VSM observations took advantage of the Curie temperature of the amorphous phase, $T_{c,\text{am}}$ of the NANOPERM alloy being less than its primary crystallization temper-

ature, T_{x1} . The magnetization is directly proportional to the volume fraction, X , of the primary α -Fe crystalline phase. The JMAK model for isothermal crystallization kinetics was compared with the Kissinger [10] model for non-isothermal crystallization kinetics using data from the three characterization methods. The activation energy for nanocrystallization of an $\text{Fe}_{88}\text{Zr}_7\text{B}_4\text{Cu}$ alloy was determined to be in the range of $Q = 2.8$ – 3.4 eV, with the crystallization kinetics determined as proceeding by immediate nucleation and 3-D diffusive growth, with the morphology index $n = 1.5$.

6. Nanocrystallization of HITPERM alloys

HITPERM alloys ($\text{Fe}_{1-x}\text{Co}_x$) $_{88}\text{M}_7\text{B}_4$ (Cu) (M = Nb, Zr, Hf, Ta) are currently being investigated by our group [24,25]. Fe and Co are the ferromagnetic species. The composition x , is important in determining the magnetic induction. Fe and Co do not partition uniformly between the nanocrystals and residual matrix, Co shows a preference for the matrix, this has important implications for increasing the Curie temperature of the amorphous phase. Most early data considers $x = 0.5$ where it has been definitively shown that the FeCo nanocrystals have an ordered B2 structure [27]. APFIM and TEM studies on HITPERM [26] show FeCo nanocrystalline grains to nucleate in the amorphous precursor without the need for Cu as a nucleation agent. Glass-forming elements segregate to the intergranular phase in a fashion similar to other nanocrystalline alloys and act to impede nanocrystal growth. Crystallography and microstructure have been studied by X-ray diffraction, synchrotron X-ray diffraction, X-ray absorption fine structure [26,27] atom probe field ion microscopy (APFIM) [25], transmission electron microscopy (TEM) and high resolution transmission electron microscopy (HRTEM).

Modifications have been made to the HITPERM composition to explore the effects on crystallization kinetics. Additions of Mo and Ta to the base HITPERM composition have been reported previously [25]. In new alloys Nb was substituted for Zr in some alloys, as well as Si and Al being substituted for B. Differential calorimetry

was used to examine crystallization kinetics. Heating rates ranged between 5 and 40 °C/min. The Kissinger analysis was employed to calculate activation energies for primary crystallization. Activation energies of 2.7–3.8 eV were determined. The base HITPERM composition has an activation energy of 3.8 eV/atom. Increasing electron concentration by substituting Nb or Mo for Zr was seen to decrease the activation energy. Removing Co was observed to decrease the activation energy.

TEM and HRTEM studies were performed on as-cast and partially crystallized HITPERM ($\text{Fe}_{44.5}\text{Co}_{44.5}\text{Zr}_7\text{B}_4$) samples. The samples were prepared as cross-sectional specimens and examined with a TECNAI F20 200 keV microscope. The as-cast sample was observed to be partially crystalline near the side of the ribbon that solidified farthest from the wheel (Fig. 3(a)). Nanocrystalline grains were observed to extend 100–500 nm into the ribbon. This is in agreement with other observed surface crystallization in this type of nanocrystalline alloy [28]. The side of the ribbon that solidified closest to the wheel was observed to be mostly amorphous, with some regions containing isolated nanocrystalline grains that appeared in HRTEM (Fig. 3(b)). The as-cast ribbon interior was observed to be amorphous.

To investigate surface crystallization, EDX spectra for Fe, Co and Zr were collected in a line leading from the interior to the free surface side of the ribbon. It was found that the Fe and Co composition remained uniform but the Zr

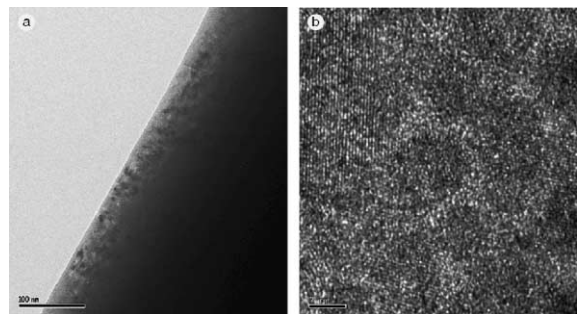


Fig. 3. (a) Cross sectional bright-field TEM of as-cast HITPERM near free side. (b) HRTEM image of roll-side of as-cast sample.

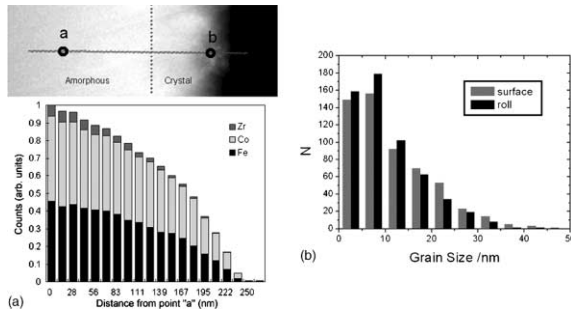


Fig. 4. (a) Cross sectional bright-field TEM of as-cast HITPERM near free side. (b) HRTEM image of roll-side of as-cast sample.

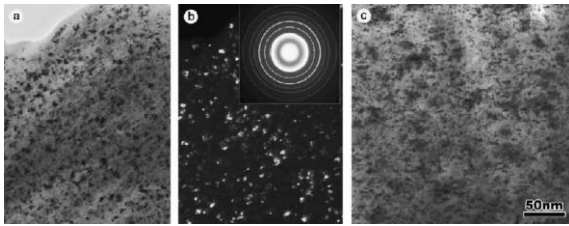


Fig. 5. (a) Typical HITPERM microstructure, after (20% volume fraction nanocrystals) nanocrystallization. (b) DF image and electron diffraction pattern of the same and (c) 3-window Zr EELS spectra showing Zr distribution (dark spots) in amorphous matrix.

concentration decreased near the surface side of the ribbon (Fig. 4(a)). It follows that the glass-forming ability of the alloy was reduced near the surface of the alloy, leading to nucleation of grains. Sporadic crystallization near the roll side of the ribbon is attributed to the presence of air gaps between the solidifying ribbon and copper chill roll locally lowering the quench rate. A partially crystallized ribbon sample was prepared by heating an as-cast specimen in a DSC for 1000 s at 500 °C (~20% crystallization was inferred from thermomagnetic measurements of similar NANOPERM alloys). Conventional TEM shows a distribution of nanocrystalline grains embedded in an amorphous matrix. Importantly, the grain diameter distribution (Fig. 4(b)) near the roll and free sides of the ribbon are similar. This indicates that nucleation proceeds uniformly across the ribbon.

A typical HITPERM microstructure, after (20% volume fraction, nanocrystals) nanocrystalliza-

tion, is shown in Fig. 5(a) with a DF image and electron diffraction pattern shown in Fig. 5(b). Fig. 5(c) shows an EELS spectra for Zr overlaid on a BF TEM image. Zr is seen to be prevalent at the interface between the nanocrystalline grains and the amorphous matrix. A similar observation for NANOPERM was made by Zhang et al. [29] using an APFIM. These observations support a model of Zr collecting in front of the growth interface.

Acknowledgements

The authors gratefully acknowledge support from the following sources: Air Force Office of Scientific Research, Air Force Materiel Command, USAF, under grant no. F49620-96-1-0454. NASA Graduate Student Researcher Fellowship under grant no. NGT3-52379. ABB Inc. and Magnetics, a division of Spang & Co.

References

- [1] Yoshizawa Y, Oguma S, Yamauchi K. *J Appl Phys* 1988;64:6044–6.
- [2] Suzuki K, Makino A, Kataika N, Inoue A, Masumoto T. *Mater Trans JIM* 1991;32:93.
- [3] Willard MA, Huang M-Q, Laughlin DE, McHenry ME, Cross JO, Harris VG, Franchetti C. *J Appl Phys* 1999;85:4421.
- [4] McHenry ME, Willard MA, Laughlin DE. *Prog Mater Sci* 2001;44:291.
- [5] Herzer G. *IEEE Trans Magn* 1990;26:1397.
- [6] Herzer G. *Phys Scrip T* 1993;49:307.
- [7] Johnson WA, Mehl RF. *RF Trans Am Inst Miner (Metall) Eng* 1939;135:227.
- [8] Avrami MJ. *MJ Phys Chem* 1939;7:1103; 1940;8:212; 1941;9:177.
- [9] Kolmogorov AN. *Bull Acad Sci USSR, Phys Ser* 1937;3:355.
- [10] Kissinger H. *Anal Chem* 1957;29:1702.
- [11] Suzuki K, Makino A, Tsai AP, Inoue A, Masumoto T. *Mater Sci Eng A* 1994;179:501.
- [12] Lecaude N, Perron JC. *Mater Sci Eng A* 1997;226–228:581–5; N. Lecaude, J.C. Perron, Proceedings of the International Symposium on Metastable, Mechanically Alloyed and Nanocrystalline Materials, vol. 269–272. Materials Science Forum, Enfield, N.H., USA: Trans Tech Publ; 1998.

- [13] Ayers JD, Harris VG, Sprague JA, Elam WT, Jones HN. *Acta Mater* 1998;46:1861.
- [14] Hono K, Hiraga K, Wang Q, Inoue A, Sakurai T. *Acta Met Mater* 1992;40:2137.
- [15] Koster U, Herold U. In: *Glassy metals I: Topics in physics*, vol. 46. Berlin: Springer-Verlag; 1981.
- [16] Luborsky F, Lieberman H. *Appl Phys Lett* 1978;33:233.
- [17] Ramanan VRV, Fish G. *JAP* 1982;53:2273.
- [18] Donald IW, Davies HA. *Phil Mag A* 1980;42:277.
- [19] Ohnuma M, Hono K, Linderoth S, Pedersen JS, Yoshizawa Y, Onodera H. *Acta Mater* 2000;48:4783.
- [20] Paoletti A, Passari L. *Nuovo Cimento* 1964;32:25.
- [21] Hsiao A, McHenry ME, Laughlin DE, Kramer MJ, Ashe C, Okubo T. *Intermag* (Amsterdam), Invited, *IEEE Trans Mag* 2002;38:2946–8.
- [22] Kramer MJ, Margulies L, McCallum RW. *Rev Sci Inst* 1999;70:3554.
- [23] Koster U, Schunemann U, Blank-Bewersdorff M, Brauer S, Sutton M, Stephenson GB. *Mater Sci Eng A* 1991;133:611.
- [24] Johnson F, Hughes P, Gallagher R, Laughlin DE, McHenry ME, Willard MA, et al. *IEEE Trans Magn* 2001;37:2261.
- [25] Johnson F, Hsiao A, Ashe C, Laughlin D, Lambeth D, McHenry M, et al. *Magnetic nanocomposites for high temperature applications*, Proceedings of the 1st IEEE Conference on Nanotechnology, Maui, HI, 28–30 October 2001.
- [26] Ping DH, Wu YQ, Hono K, Willard MA, McHenry ME, Laughlin DE. *Scripta Mater* 2001;45:781.
- [27] Willard MA, Gingras M, Lee MJ, Harris VG, Laughlin DE, McHenry ME. *MRS Res Symp Proc* 1999;577:469.
- [28] Ayers JD, Konert JH, Dantonio P, Pattnaik A, Vold CL, Jones HN. *J Mat'l Sci* 1995;30:4492.
- [29] Zhang Y, Hono K, Inoue A, Sakurai T. *Scripta Mater* 1996;34:1705.